catalysts

MDPI

Article

Soot Oxidation over γ-Al_2O_3-Supported Manganese-Based Binary Catalyst in a Dielectric Barrier Discharge Reactor

Xinbo Zhu [1,*], Xiqiang Wu [1,2], Jin Liu [1], Jianbin Luo [1], Zhengda Yang [3], Ye Jiang [3] and Geng Chen [1]

[1] Faculty of Maritime and Transportation, Ningbo University, Ningbo 315211, China; wuxiqiang96@foxmail.com (X.W.); a853800339@126.com (J.L.); ljb15667840050a@163.com (J.L.); chengeng@nbu.edu.cn (G.C.)
[2] Department of Device Development, CRRC New Energy Technology Co., Ltd., Ningbo 315112, China
[3] College of New Energy, China University of Petroleum (East China), Qingdao 266580, China; yzd019@upc.edu.cn (Z.Y.); jiangye@upc.edu.cn (Y.J.)
* Correspondence: zhuxinbo@nbu.edu.cn

Abstract: In this work, soot oxidation was conducted over a series of Mn-X/γ-Al_2O_3 (M = Ce, Co and Cu) binary catalysts in a dielectric barrier discharge reactor. The soot conversion in the plasma–catalytic system was in the order of Mn/γ-Al_2O_3 (57.7%) > Mn-Co/γ-Al_2O_3 (53.9%) > Mn-Ce/γ-Al_2O_3 (51.6%) > Mn-Cu/γ-Al_2O_3 (47.7%) during the 30 min soot oxidation process at 14 W and 150 °C. Meanwhile, the doping of Ce, Co and Cu slightly improved the CO_2 selectivity of the process by 4.7% to 10.3% compared to soot oxidation over Mn/γ-Al_2O_3.It is worth to note that the order of CO_2 selectivity was in the opposite order with soot oxidation rate. The effects of discharge power, oxygen content in the carrier gas and reaction temperature on plasma–catalytic soot oxidation was systematically analyzed. The catalyst characterizations, including N_2 adsorption–desorption, X-ray diffraction, X-ray photoelectron spectroscopy, temperature-programmed reduction by H_2 and temperature-programmed desorption of O_2, were conducted to illustrate the reaction mechanisms of plasma–catalytic soot oxidation and reaction pathways.

Keywords: plasma–catalysis; soot oxidation; manganese-based oxides; transition metal; binary catalyst

Citation: Zhu, X.; Wu, X.; Liu, J.; Luo, J.; Yang, Z.; Jiang, Y.; Chen, G. Soot Oxidation over γ-Al_2O_3-Supported Manganese-Based Binary Catalyst in a Dielectric Barrier Discharge Reactor. *Catalysts* **2022**, *12*, 716. https://doi.org/10.3390/catal12070716

Academic Editors: Huijuan Wang and He Guo

Received: 5 June 2022
Accepted: 23 June 2022
Published: 29 June 2022

1. Introduction

The diesel engine is widely used as a modern power source due to its advantages in power, fuel economy and high reliability compared to gasoline engines. However, particulate matter (mainly soot, namely elemental carbon) emissions from diesel engines could result in an acute impact on both human health and the environment [1]. In practice, diesel engine filters (DPFs) are used to capture soot and meet the stringent emission legislations for diesel engines. The captured soot is further oxidized for DPF regeneration at the exhaust temperature via many methods, including catalytic regeneration, fuel burners, external heating and recirculation of exhaust gas [2,3]. Among these methods, catalytic DPF regeneration is promising since the ignition temperature could be reduced to 400–500 °C compared with the temperature of above 600 °C without a catalyst [4,5]. However, the ignition temperature is still significantly higher than the exhaust temperature of engines, especially for the idling working conditions [6,7]. Thus, the catalytic regeneration of DPFs could not work properly under these conditions.

To overcome the drawbacks of catalytic DPF regeneration at low temperatures, plasma–catalysis has emerged as a promising method due to its unique characteristics of a compact system, quick response and mild reaction conditions [8–10]. In typical air plasma, highly energetic electrons (1 eV to 10 eV) could be generated. The electrons could then collide with background gas molecules to generate short-lived chemically reactive radicals (e. g., O· and O_3) for soot oxidation. However, the relatively low surface area of soot particles makes it difficult to achieve both a high soot oxidation rate and CO_2 selectivity of the process in

cases of using plasma alone [9,11]. The integration of plasma and a heterogeneous catalyst, also known as "plasma catalysis", could result in a synergistic effect since the short-lived radicals play a crucial role in activating effective collisions between oxidative species and soot on catalyst surfaces [12].

The composition of a catalyst imposes significant effects on the reaction performance of plasma–catalysis, including gas-phase pollutant removal, NH_3 synthesis, water purification, steam reforming, etc. [13,14]. As for soot oxidation, Ranji-Burachaloo reported the soot oxidation rate in a pin-to-plate plasma reactor over Mn, Fe and Co oxides. The CO_2 selectivity of the process reached the maximum values of 90%, 85% and 79% at the discharge power of 7.4 W and 350 °C, while energy yields of soot conversion were 7.0, 6.0 and 5.6 g kWh^{-1}, respectively [10]. Liu et al. found that the synergistic effect between plasma and $LaAgMnCoO_3$ perovskite could greatly improve the soot oxidation below 200 °C in a dielectric barrier discharge (DBD) plasma reactor. The soot conversion and CO_2 selectivity were 63% and 90% in a plasma–$LaAg_{0.2}MnCo_{0.2}O_3$ system, respectively, compared to 14% and 75% in the plasma–$LaMnO_3$ system [15]. Manganese has shown potential as the active metal of catalytic oxidation of volatile organic compound oxidation and soot [16,17]. Chen et al. prepared a series of MnO_x/wire-mesh monoliths for soot oxidation. The sample calcined at 700 °C showed a T_{90} value of 421 °C and CO_2 selectivity of 93.2%, which were significantly improved compared with 618 °C and 46.5% for pure soot oxidation [18]. Yu et al. reported that the T_{90} value of the $MnCe_1O_x$ catalyst (370 °C) was 237 °C lower than that of pure soot, while the CO_2 selectivity (99.6%) was 47.2% higher compared to that of pure soot [19]. However, there is very limited literature on plasma–catalytic soot oxidation over Mn-based catalysts to the best of the authors' knowledge, so the effect of various reaction factors on the reaction performance and the underlying mechanisms are not fully understood [20].

In this work, three kinds of Mn-X/γ-Al_2O_3 (X = Ce, Co and Cu) catalysts were prepared using wet impregnation method for soot oxidation in a DBD plasma reactor, while the effects of various parameters on plasma–catalytic soot oxidation were analyzed. A series of catalyst characterizations, including N_2 adsorption–desorption, X-ray diffraction, X-ray photoelectron spectrum, temperature-programmed reduction by H_2 (H_2-TPR) and temperature-programmed desorption of O_2 (O_2-TPD), were conducted to illustrate the textural and chemical properties of the Mn-X/γ-Al_2O_3 catalysts. The correlations between plasma-induced soot oxidation performance and the catalyst properties were discussed together with the underlying mechanisms.

2. Results and Discussions

2.1. Textural Properties of Mn-X/γ-Al_2O_3 Catalysts

Table 1 shows the specific surface area, pore volumes and average pore diameter of the Mn-X/γ-Al_2O_3 (X = Ce, Co and Cu) catalysts. All catalysts possessed type V isotherms and H4-type hysteresis loops, indicating the existence of narrow slit-like pores in the Mn-X/γ-Al_2O_3 catalyst, and the loading of active metal did not significantly affect the textural properties of the γ-Al_2O_3 support [21,22]. The specific surface area (S_{BET}) of pure γ-Al_2O_3 was 224.6 $m^2 \cdot g^{-1}$, while its pore volume and average pore diameter were 0.39 $cm^3 \cdot g^{-1}$ and 6.9 Å. The doping of Mn species slightly decreased the S_{BET} value to 207.6 $m^2 \cdot g^{-1}$, and the S_{BET} value further decreased to between 171.4 $m^2 \cdot g^{-1}$ and 192.5 $m^2 \cdot g^{-1}$ after promoter (Ce, Co or Cu species) doping. The pore volume of the Mn-X/γ-Al_2O_3 catalysts (0.34–0.37 $cm^3 \cdot g^{-1}$) was slightly lower than that of Mn/γ-Al_2O_3 (0.38 $cm^3 \cdot g^{-1}$) and the pure γ-Al_2O_3 support (0.39 $cm^3 \cdot g^{-1}$). The doping of active metal on the γ-Al_2O_3 support may not have covered the γ-Al_2O_3 surface and partly blocked the pores within the γ-Al_2O_3 support, leading to the decrease in the S_{BET} value and pore volume of the Mn-X/γ-Al_2O_3 catalysts. As for the average pore diameter, the values for Mn-X/γ-Al_2O_3 catalysts (7.4–7.9 Å) were slightly higher than that of γ-Al_2O_3 (6.9 Å). This phenomenon could be attributed to the clogging of pores with a small diameter within γ-Al_2O_3 after active metal loading. Similar results were reported in our previous work and by Zakaria et al. [23].

Table 1. Physicochemical properties of the Mn-X/γ-Al_2O_3 catalysts.

Sample	S_{BET} ($m^2 \cdot g^{-1}$)	Total Pore Volume ($cm^3 \cdot g^{-1}$)	Average Pore Diameter (Å)	$O_{ads}/(O_{ads}+O_{latt})$ (%)	H_2 Consumption (mmol g^{-1})	O_2 Desorption (mmol g^{-1})	
						<350 °C	>350 °C
MnO_x/γ-Al_2O_3	208	0.38	7.4	77.8	0.36	0.69	2.50
Mn-Ce/γ-Al_2O_3	190	0.37	7.9	74.9	0.35	0.71	1.66
Mn-Co/γ-Al_2O_3	193	0.37	7.7	75.8	0.37	1.05	1.83
Mn-Cu/γ-Al_2O_3	171	0.34	7.8	72.0	0.35	0.93	2.14

The XRD patterns of the Mn-X/γ-Al_2O_3 catalysts are given in Figure 1. The main diffraction peaks of all Mn-X/γ-Al_2O_3 and Mn/γ-Al_2O_3 catalysts at the 2θ of 37.6°, 45.9° and 67.0° were in good agreement with the cubic structure of pure γ-Al_2O_3 (JCPDS No. 00-010-0425), indicating that the crystalline structure of γ-Al_2O_3 was maintained after active metal doping. The intensities of diffraction peaks for Mn-X/γ-Al_2O_3 catalysts were slightly lower than that of pure γ-Al_2O_3, which could be ascribed to the dispersion of dopants on the surface of the support, and part of the dopants may have entered the crystal form of the support and formed a solid solution [24,25]. The diffraction peaks at 42.8° belonged to the MnO_2 phase (JCPDS No. 03-065-2821), which were observed for the four catalysts. In addition, weak diffraction peaks of CeO_2 (JCPDS No. 03-065-5923), Co_3O_4 (JCPDS No. 00-042-1467) and CuO (JCPDS No. 01-089-5899) could be found in the corresponding XRD pattern, indicating that active metal oxides existed in the form of crystallites on the γ-Al_2O_3 support. Moreover, Mn-Ce/γ-Al_2O_3 showed strong diffraction peaks of CeO_2 species. The crystalline sizes of the Mn, Ce, Co and Cu oxides were 5.2 nm, 4.3 nm, 3.7 nm and 7.6 nm, respectively, as calculated using the Scherrer equation. The small particle sizes would benefit the heterogeneous catalytic reactions [26].

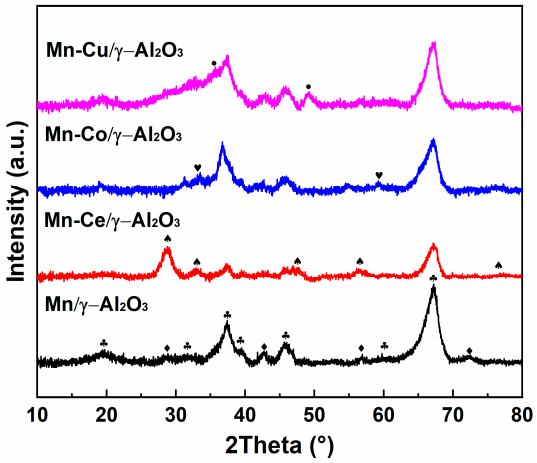

Figure 1. XRD patterns of the Mn-X/γ-Al_2O_3 catalysts: ♣ γ-Al_2O_3, ♦ MnO_2, ♥ Co_3O_4, ♠ CeO_2 and • CuO.

2.2. Chemical Properties of Mn-X/γ-Al_2O_3 Catalysts

XPS was performed to investigate the valence and relative content of each element on the catalyst surface. The O 1s XPS spectra of the Mn-X/γ-Al_2O_3 catalysts are presented in Figure 2. The O 1s spectra could be deconvoluted into two major peaks. The peaks around 531.3 eV corresponded to the surface-adsorbed oxygen (O_{ads}), while the peaks around 529.6 eV could be ascribed to lattice oxygen (O_{latt}) species [27]. The relative concentrations of $O_{ads}/(O_{ads}+O_{latt})$ over the four catalysts are listed in Table 1. The $O_{ads}/(O_{ads}+O_{latt})$ value slightly decreased by 2.0–5.8% after the doping of Ce, Co and Cu on the Mn/γ-Al_2O_3 catalyst compared with Mn/γ-Al_2O_3 (77.8%), while the highest $O_{ads}/(O_{ads}+O_{latt})$ value of

75.8% was observed over Mn-Co/γ-Al_2O_3 among the Mn-X/γ-Al_2O_3 catalysts. It is widely reported that the O_{ads} species are closely related to the oxygen vacancies on the catalyst surface. As a result, the catalyst with a higher $O_{ads}/(O_{ads}+O_{latt})$ value would effectively promote the performance of heterogeneous catalytic reaction [28].

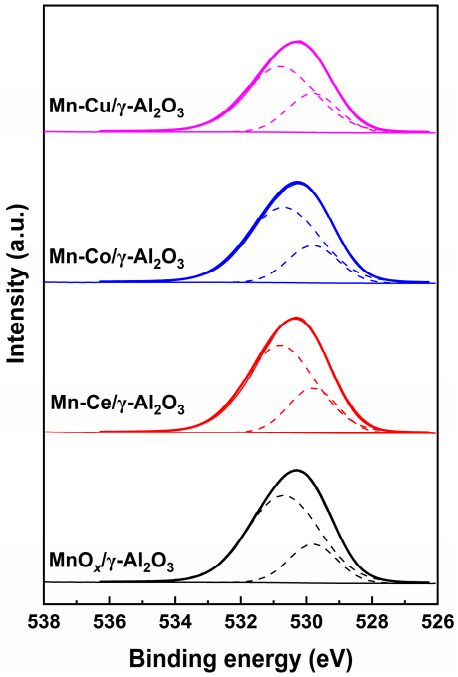

Figure 2. XPS spectra of O 1s for Mn-X/γ-Al_2O_3 catalysts.

The reducibility of the Mn-X/γ-Al_2O_3 catalysts was analyzed through a H_2-TPR experiment (Figure 3). The H_2-TPR profiles of Mn/γ-Al_2O_3 showed two major reduction peaks at 297 °C and 410 °C. As the pure γ-Al_2O_3 support had no reduction peak between 100 °C and 600 °C [29], the first reduction peak could be attributed to the reduction of Mn^{4+} to Mn^{3+}, while the second peak belonged to the reduction of Mn^{3+} to Mn^{2+} species [30]. The doping of Ce, Co and Cu significantly changed the reduction behavior of Mn-X/γ-Al_2O_3 catalysts. For Mn-Ce/γ-Al_2O_3, the two reduction peaks shifted to lower temperatures of 290 °C and 357 °C, respectively, indicating the mutual effect between Mn and Ce species on the catalyst surface [31]. In the case of Mn-Cu/γ-Al_2O_3, the predominant reduction peaks were observed at 276 °C and 362 °C, which could be ascribed to the reduction of Cu^{2+} and Mn^{4+} species [32]. The H_2-TPR profile of Mn-Co/γ-Al_2O_3 showed a broad peak between 272 °C and 379 °C, which belonged to the reduction of Mn^{4+} and Co^{3+} [24]. The lower reduction temperatures implied better oxygen mobility of the Mn-Co/γ-Al_2O_3 and Mn-Cu/γ-Al_2O_3 catalysts compared with Mn-Ce/γ-Al_2O_3 and Mn/γ-Al_2O_3 catalysts. To gain a better insight into reducibility, H_2 consumption of the catalysts was calculated (Table 1). It could be observed that all four catalyst samples exhibited a similar H_2 consumption amount due to the fixed loading amount of metal dopants. It could be deduced that the reducibility of Mn-Co/γ-Al_2O_3 and Mn-Cu/γ-Al_2O_3 was much better than that of Mn-Ce/γ-Al_2O_3 and Mn/γ-Al_2O_3 catalysts, taking the reduction temperature and H_2 consumption amount into consideration.

O_2-TPD experiments were conducted to study the nature of surface oxygen species, as shown in Figure 4. The O_2-TPD profiles for the four catalysts were quite similar. The desorption peaks between 100 °C and 350 °C were attributed to the adsorbed surface oxygen species (α-O_2) on oxygen vacancies, while the peaks between 350 °C and 700 °C belonged to chemically adsorbed oxygen species (β-O_2) [33]. The surface oxygen species would go through the transformation process of O_2(ad) → O_2^-(ad) → O^-(ad) → O_2^-(ad/latt) via electron gaining [34]. The O_2 desorption amount is presented in Table 1, while the peaks

above 750 °C, which could be assigned to lattice oxygen, were not observed in this work. Compared with pure γ-Al_2O_3, the peak areas of α-O_2 for Mn-X/γ-Al_2O_3 catalysts were in the range of 0.71 mmol·g^{-1} to 1.05 mmol·g^{-1}, which were much higher than that of Mn/γ-Al_2O_3 (0.69 mmol·g^{-1}). The highest α-O_2 value was obtained over the Mn-Co/γ-Al_2O_3 catalyst. On the other hand, the peak areas of β-O_2 for Mn-X/γ-Al_2O_3 catalysts were lower than that of Mn/γ-Al_2O_3. These results are in accordance with the XPS spectra and H_2-TPR profiles. The adsorbed oxygen species (O_{ads}) are closely associated with the oxygen vacancies and oxygen mobility on catalyst surfaces, which could in turn contribute to the process of soot oxidation on the catalyst surfaces in the presence of plasma discharge [35].

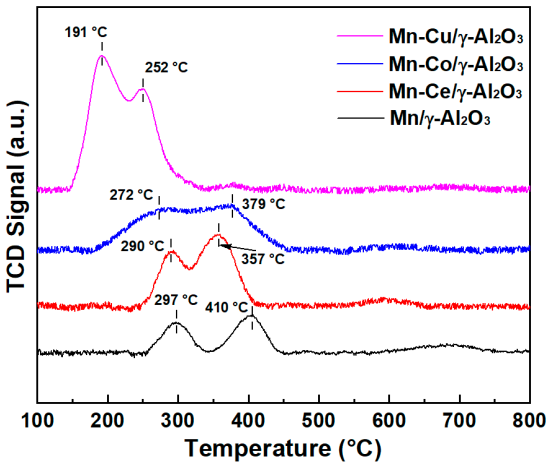

Figure 3. H_2-TPR profiles of Mn-X/γ-Al_2O_3 catalysts.

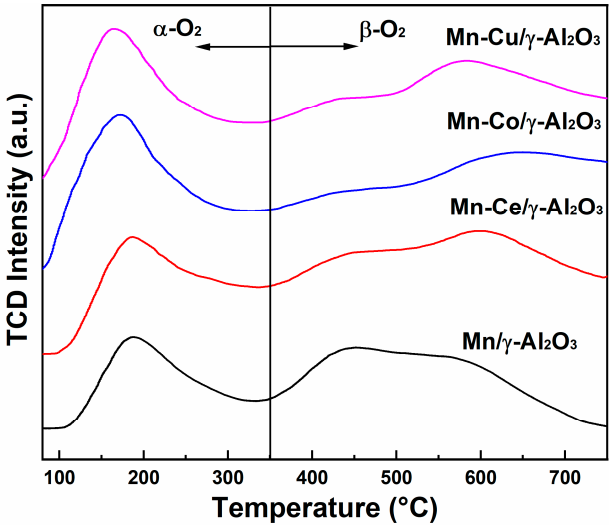

Figure 4. O_2-TPD profiles of Mn-X/γ-Al_2O_3 catalysts.

2.3. Effect of Catalyst Composition

Figure 5 shows the effect of catalyst composition on plasma–catalytic soot oxidation in terms of the oxidation rate and CO_2 selectivity as a function of reaction time. The soot oxidation increased over time for all plasma reactors with Mn-X/γ-Al_2O_3 catalyst-packing, while the CO_2 selectivity of the process showed only a 0.5% to 1.0% improvement within the 30 min soot oxidation process. The soot oxidation rate of the undoped Mn/γ-Al_2O_3 catalyst was higher than that of the Mn-X/γ-Al_2O_3 catalysts. The relative low soot oxidation rate could be ascribed to the duration of the reaction period, which takes about 60 min to achieve 100% soot oxidation as reported in our previous work [36]. For example, the soot oxidation rate reached 53.9% for the Mn-Co/γ-Al_2O_3-packed plasma reactor, followed

by Mn-Ce/γ-Al_2O_3 (51.6%) and Mn-Cu/γ-Al_2O_3 (47.7%) after the 30 min reaction. In contrast with the soot oxidation rate, the CO_2 selectivity of the plasma–catalytic process followed the order of Mn/γ-Al_2O_3 (59.8%) < Mn-Co/γ-Al_2O_3 (64.5%) < Mn-Ce/γ-Al_2O_3 (64.8%) < Mn-Cu/γ-Al_2O_3 (70.1%). It is worthy to note that the soot oxidation rate and CO_2 selectivity of Mn/γ-Al_2O_3 were close to those of the Mn-Co/γ-Al_2O_3 catalyst.

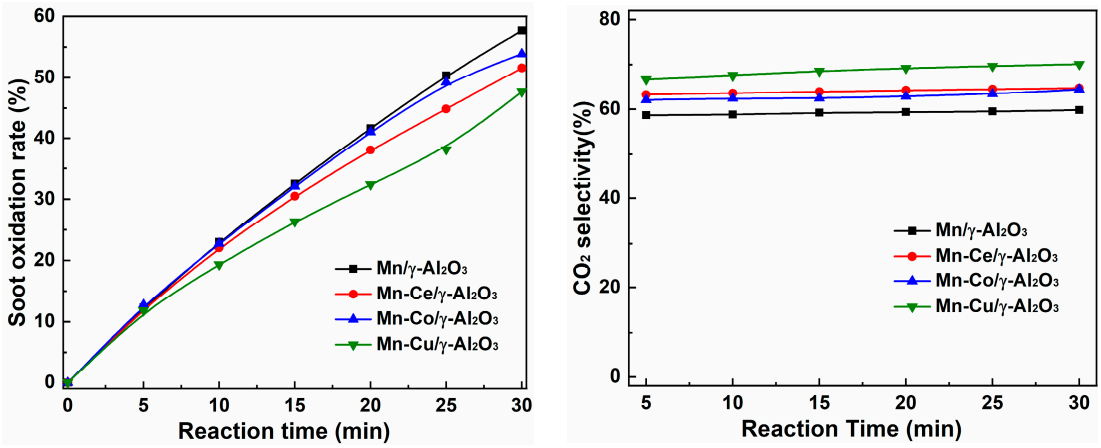

(**a**) (**b**)

Figure 5. Effect of Mn-X/γ-Al_2O_3 (X = Ce, Co and Cu) on plasma–catalytic soot oxidation: (**a**) oxidation rate and (**b**) CO_2 selectivity (discharge power: 14 W, reaction temperature: 150 °C, oxygen content: 10 vol.% and gas flow rate: 500 mL·min^{-1}).

In plasma region, the soot oxidation was initiated by the plasma-generated energetic electrons and reactive radicals, including O·, O_3, etc., while the generation of these species was directly associated with the energy deposited into the DBD plasma reactor [8,10]. In the presence of catalyst pellets and/or soot particles, the discharge mode of DBD plasma would be the combination of filamentary micro-discharge in the gas phase and surface discharge along the surfaces of packed catalysts and soot particles [37]. Moreover, the plasma discharge region would be extended and intensified within the packed-bed layer, which could contribute to the generation of reactive species. Once generated, these species would be transported onto the external surfaces of soot particles and further oxidize the soot particles to CO and CO_2 [38]. It is worth noting that the activation energy of soot oxidation to CO (ΔH = −110 kJ·mol^{-1}) (Reaction (1)) is only 27.9% that of soot oxidation to CO_2 (ΔH = −394 kJ·mol^{-1}) (Reaction (2)) [39]. Consequently, the possibilities of CO formation were much higher than for CO_2 in plasma-induced soot oxidation, which led to the low CO_2 selectivity of the process. In addition, the direct oxidation of CO to CO_2 was also expected both in the gas phase and on the surfaces of the catalyst or soot.

$$C_{soot} + O \rightarrow CO \quad (1)$$

$$C_{soot} + O_3 \rightarrow CO + O_2 \quad (2)$$

$$C_{soot} + O \rightarrow CO_2 \quad (3)$$

$$C_{soot} + O_3 \rightarrow CO_2 + O_2 \quad (4)$$

$$CO + O \rightarrow CO_2 \quad (5)$$

$$CO + O_3 \rightarrow CO_2 + O_2 \quad (6)$$

In the packed-bed DBD reactor, besides soot oxidation by O· radicals and O_3 from the gas phase, the soot oxidation could be promoted by the active sites on the surfaces of Mn-X/γ-Al_2O_3 via the soot–catalyst contact points. Moreover, the oxidation of CO to CO_2 may also be improved via the soot–catalyst contact points. It is well-known that the properties

of catalysts would significantly affect the reaction performance of plasma–catalytic soot oxidation. Previous work also confirmed that the activated oxygen species on the catalyst surfaces can participate in the oxidation of soot and CO to form CO_2 [40]. In addition, the transfer of oxygen species to the surfaces of soot via the physical contact points is also one of the major roles of Mn-X/γ-Al_2O_3 catalysts [41]. The N_2 adsorption–desorption results show that the S_{BET}, pore volume and pore diameters of Mn-X/γ-Al_2O_3 and Mn/γ-Al_2O_3 catalysts were slightly lower than those of the γ-Al_2O_3 support. In the loose-contact mode, the contact between the catalyst pellets and soot was at the scales of μm-size and mm-size rather than at the nanoscale. It could be deduced that the textural properties of the catalysts may not play a vital role in improving plasma-induced soot oxidation.

For the binary Mn-X/γ-Al_2O_3 catalysts, the catalytic active sites introduced by the dopants would contribute to the soot oxidation as confirmed by the improved redox properties of Mn-X/γ-Al_2O_3 [42,43]. The XPS spectra of O 1s showed improved $O_{ads}/(O_{ads}+O_{latt})$ values over Mn-X/γ-Al_2O_3 compared to those of Mn/γ-Al_2O_3. The presence of O_{ads} was correlated with the formation of oxygen vacancies on catalyst surfaces. The oxygen vacancies on Mn-X/γ-Al_2O_3 could act as the reservoir of O_{ads} species and O· radicals generated by plasma [44]. The O_2-TPD profiles evidenced that the O_{ads} was the major oxygen species on the surfaces of the Mn-X/γ-Al_2O_3 catalysts, and the order of O_{ads} amount was Mn-Co/γ-Al_2O_3 > Mn-Cu/γ-Al_2O_3 > Mn-Ce/γ-Al_2O_3 > Mn/γ-Al_2O_3. The complete soot oxidation strongly depends on the oxygen adsorption capacity of the supported metal oxide catalysts and the facilitated oxygen transfer from catalyst surfaces to soot particles [45]. In plasma region, the catalysts with higher $O_{ads}/(O_{ads}+O_{latt})$ values may be beneficial for soot oxidation since O_{ads} possessed better mobility compared to O_{latt} species, and it is much easier to release and transport O_{ads} species to the surface of soot particles near the interfaces between soot particles and catalyst pellets (i.e., via the contact points) [19]. The H_2-TPR profiles also showed the best reducibility of Mn-Co/γ-Al_2O_3 among the tested Mn-X/γ-Al_2O_3 catalysts, while the oxygen vacancies and O_{ads} species could be refilled during the plasma process by the generated O· radicals and O_3 species. However, it could be deduced that less active sites would be effectively utilized due to the "loose contact" mode between catalyst pellets and soot since the proximity of the catalyst and soot is of great significance in the "solid-solid reaction" [46]. In the "loose contact" mode, most of the plasma-generated reactive species would be diminished before reaching the interfaces between soot and the gas phase or between soot and catalysts [8,47], especially those decomposed to O_{ads} species on the surfaces of Mn-X/γ-Al_2O_3 catalysts. The oxidation of CO to CO_2 around the contact points between the catalyst and soot would be consequently improved, leading to the formation of more CO_2 molecules and higher CO_2 selectivity in the presence of Mn-X/γ-Al_2O_3 catalysts. Similarly, Ranji-Burachaloo et al. reported that the loose-contact mode would result in a lower soot oxidation rate and CO_2 selectivity compared with the tight-contact mode [10]. A very good correlation between the CO_2 selectivity and the redox properties of Mn-X/γ-Al_2O_3 catalysts was observed in this work, while the order oxidation rate contrasted with the order of redox properties.

2.4. Effect of Operation Parameters

Figure 6 shows the effect of discharge power on the plasma–catalytic soot oxidation rate and CO_2 selectivity at the 30th min over Mn-Co/γ-Al_2O_3 and Mn/γ-Al_2O_3 catalysts. The soot oxidation rate increased from 33.4% to 71.3% in the presence of the Mn-Co/γ-Al_2O_3 catalyst in the discharge power range of 10 W to 18 W, while the value for the Mn/γ-Al_2O_3 catalyst increased from 35.1% to 78.1% in the same range. It is well-accepted that the discharge power is essential for the initial plasma-induced reactions as various types of energetic electrons and chemically reactive species (e.g., O and O_3) can be generated with the help of input discharge power [48]. The species could be transported onto the surfaces of catalyst and soot particles, resulting in the oxidation of soot and formation of CO and CO_2. In the plasma region, more micro-discharge channels would be generated at a higher discharge power, which could result in the generation of more energetic electrons

and chemically reactive species during the discharge process [13]. Consequently, the soot oxidation process could be greatly improved since the packed soot and catalyst particles could directly interact with the micro-discharge and reactive species. As with the CO_2 selectivity, the values for Mn-Co/γ-Al_2O_3 and Mn/γ-Al_2O_3 catalysts both decreased slightly by ~3.3% in the range of 10 W to 18 W. As discussed before, the oxidation of soot to CO is the predominant reaction pathway rather than the oxidation of soot to CO_2 due to the distinct difference in activation energy of these two reactions. The decrease in CO_2 selectivity could be ascribed to the formation of more CO in soot oxidation at a higher discharge power regardless of the catalyst type.

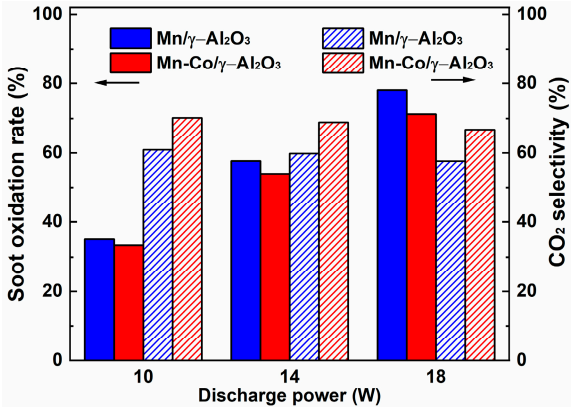

Figure 6. Effect of discharge power on plasma–catalytic soot oxidation over the Mn-Co/γ-Al_2O_3 and Mn/γ-Al_2O_3 catalysts (reaction temperature: 150 °C, reaction time: 30 min, oxygen content: 10 vol.% and gas flow rate: 500 mL·min^{-1}).

Figure 7 presents the effect of oxygen content on plasma–catalytic soot oxidation and the selectivity of CO_2 over Mn-Co/γ-Al_2O_3 and Mn/γ-Al_2O_3 catalysts. With the increase in oxygen content from 5% to 20%, the soot oxidation rate increased from 41.2% to 60.2% for Mn-Co/γ-Al_2O_3 and 43.9% to 66.5% for the Mn/γ-Al_2O_3-catalyst-packed reactor, respectively. However, the CO_2 selectivity of the process decreased very slightly from 66.5% and 61.7% at 5 vol.% oxygen content by 2.6% and 3.3% at the oxygen content of 20% for these two catalysts. Previous work reported that oxygen radicals, including O radicals and O_3, were the major oxidative species in N_2/O_2 plasma [49]. At a higher oxygen content, more oxidative species would be generated via electronic excitation for soot oxidation. As the oxidation of soot was carried out in a "gas-solid-solid" heterogeneous system, the oxidative species would participate in the oxidation of the external surface of the model soot particles and form the final products of CO and CO_2 [47]. The presence of the Mn-based catalyst would contribute to the decomposition of O_3 to O· radicals and surface-adsorbed oxygen species (O_{ads}) as reported by Zhang et al. [50]. These species could oxidize the soot particles to CO or convert the CO species in the gas phase to CO_2. Considering the low activation energy required for soot oxidation to CO compared to CO_2, it is reasonable that the CO_2 selectivity decreased with the increase in oxygen content.

The effect of the reaction temperature on plasma–catalytic soot oxidation and CO_2 selectivity at the 30th min over Mn-Co/γ-Al_2O_3 and Mn/γ-Al_2O_3 is presented in Figure 8. The soot oxidation rate decreased with the increase in reaction temperature from 25 °C to 150 °C. The soot oxidation rate decreased from 58.6% at 25 °C to 53.9 at 150 °C, while the value of the Mn/γ-Al_2O_3-catalyst-packed reactor decreased from 59.0% to 57.7% in the same temperature range. On the other hand, the CO_2 selectivity increased from 54.9% to 59.8% for the Mn/γ-Al_2O_3-packed plasma reactor, while the value for Mn-Co/γ-Al_2O_3 improved from 58.4% to 64.8%. At a higher reaction temperature, the diminish in plasma-generated reactive species would be improved due to the enhancement of the Brownian motion of these radicals via the collisions between them and the carrier gas molecules [51]. The decrease in the soot oxidation rate could be ascribed to the diminish of chemically

reactive species in the gas phase as most of these species would fail to be transported to the surfaces of soot particles and catalyst pellets at higher temperature [52–54]. However, the oxygen species on the catalyst surfaces would be slightly activated at a higher temperature, leading to the further oxidation of -CO groups on soot surfaces via the contact points between catalyst pellets and soot particles. Consequently, the formation of more CO_2 could be expected, and the CO_2 selectivity increased with the increasing reaction temperature.

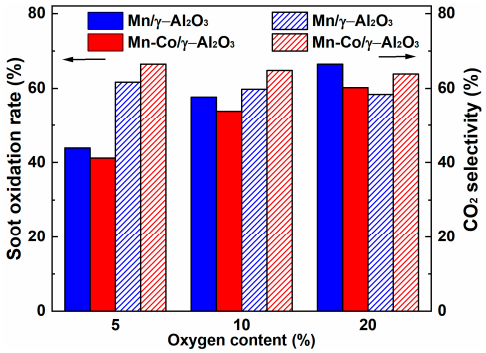

Figure 7. Effect of oxygen content on plasma–catalytic soot oxidation at 30th min over Mn-Co/γ-Al_2O_3 and Mn/γ-Al_2O_3 catalysts (discharge power: 14 W, reaction temperature: 150 °C, reaction time: 30 min and gas flow rate: 500 mL·min^{-1}).

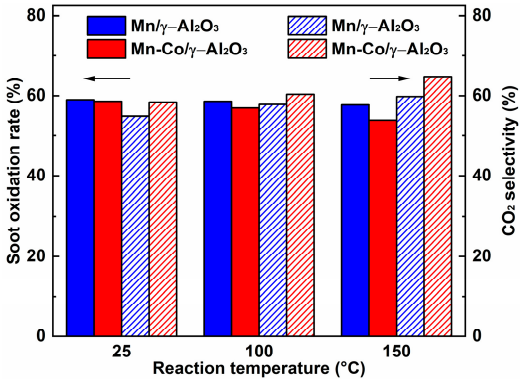

Figure 8. Effect of reaction temperature on plasma–catalytic soot oxidation at 30th min over Mn-Co/γ-Al_2O_3 and Mn/γ-Al_2O_3 catalysts (discharge power: 14 W, reaction time: 30 min, oxygen content: 10 vol.% and gas flow rate: 500 mL·min^{-1}).

3. Materials and Methods

3.1. Catalyst Characterizations

N_2 adsorption–desorption experiments were conducted at −196 °C over an Autosorb-iQ instrument from Quantachrome Co. Ltd., Boynton Beach, FL, USA. The Brunauer–Emmet–Teller specific surface area (S_{BET}) value of the Mn-X/γ-Al_2O_3 catalysts was calculated using the equation, while the pore diameters and pore volumes were calculated using the Barrett–Joyner–Hallender (BJH) method.

X-ray diffraction (XRD) patterns of the catalysts were recorded using a D/max-2000 diffractometer (Rikagu Co. Ltd., Tokyo, Japan) at 100 mA and 40 kV using a Cu-Kα radiation source. The scanning 2θ range was between 10 and 80° with the step size of 0.02°.

X-ray photoelectron spectroscopy (XPS) was performed on an ESCALAB 250Xi spectrometer (ThermoFisher Co. Ltd., Waltham, MA, USA) fitted with Al Kα radiation (hν = 1486.6 eV) X-ray source. All binding energies were calibrated to the C 1s neutral peak at 284.6 eV.

Both hydrogen temperature-programmed reduction (H_2-TPR) and oxygen temperature-programmed desorption (O_2-TPD) were conducted using an AutoChemII 2920 chemical

adsorption analyzer (Micromeritics Co. Ltd., Norcross, GA, USA). For H_2-TPR, a 50 mg sample was pretreated at 300 °C for 1 h in 30 mL·min^{-1} Ar flow and then cooled down to 50 °C. After that, the gas flow was switched to 5% H_2/Ar (30 mL·min^{-1}), and the sample was heated from 50 °C to 850 °C at a heating rate of 10 °C·min^{-1}. As for O_2-TPD, a 50 mg catalyst was purged at 250 °C for 1 h at 5% O_2/He flow rate (30 mL·min^{-1}) and subsequently cooled down to 50 °C. Then, the gas flow was switched to He (30 mL·min^{-1}), and the temperature increased linearly to 850 °C at a heating rate of 10 °C·min^{-1}.

3.2. Catalyst Preparation

In this work, the Mn-X/γ-Al_2O_3 (X = Ce, Co and Cu) catalysts were prepared using the wet impregnation method. All reagents including metal nitrates and γ-Al_2O_3 were purchased from Aladdin Co. Ltd. and of analytic grade. Firstly, weighted metal nitrates were dissolved in deionized water to obtain a solution with the metal ion concentration of 0.1 mol·L^{-1}. Secondly, the desired amount of γ-Al_2O_3 was added to the metal ion solution and magnetically stirred for 4 h at 80 °C. Then, the samples were dried in an oven at 110 °C for 12 h and calcined at 500 °C for 5 h. Finally, the obtained catalysts were crashed and sieved to 40 to 60 meshes prior to use. The loading amount of metal ions was 5% in weight, while the weights of Mn and the dopants were both 2.5 %. In addition, the Mn/γ-Al_2O_3 catalyst with the same loading amount (5% in weight) was prepared with the same procedure for comparison.

3.3. Experimental Setup

The diagram of the experimental setup for plasma–catalytic soot oxidation is shown in Figure 9. In this work, all carrier gases (purity > 99.99%, N_2 and O_2) were supplied from gas cylinders purchased from Fangxin Co. Ltd., China. The gas streams were regulated by mass flow controllers (Sevenstars D07-B, China), while the total gas flow rate was typically 500 mL min^{-1} with a N_2/O_2 molar ratio of 9:1. Before being introduced into the DBD plasma reactor, the gas streams were premixed.

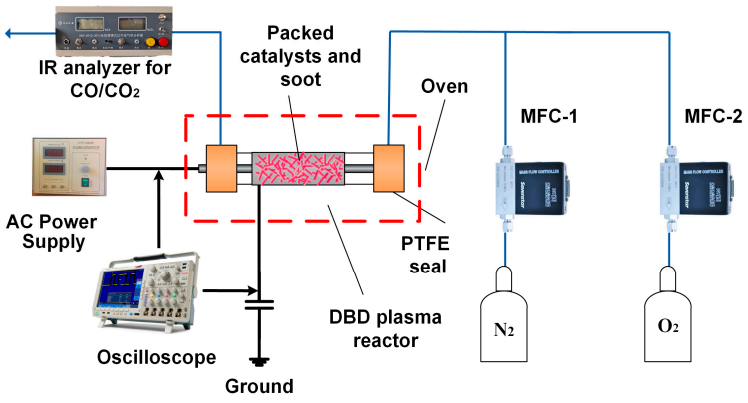

Figure 9. Experimental setup of plasma–catalytic soot oxidation.

The DBD plasma reactor consisted of a quartz tube, a stainless-steel rod, a stainless-steel net and two PTFE caps. The inner diameter of the quartz tube was 9 mm, while the wall thickness was 1.5 mm. The stainless-steel rod with a 4 mm diameter was fixed at the axis of the quartz tube by the PTFE seals. The stainless-steel rod was connected to a CTP-2000 K high-voltage power supply (Suman, Nanjing, China) as a high-voltage electrode. A stainless-steel mesh was wrapped outside the quartz tube and acted as the ground electrode. The resulting discharge gap and discharge length were 2.5 mm and 30 mm. Before the experiments, typical Printex-U soot (Degussa Co. Ltd., Frankfurt, Germany) was mixed with the Mn-X/γ-Al_2O_3 catalyst in a mortar for 10 min to obtain a loose contact between soot and catalyst particles. The weight ratio of soot to Mn-X/γ-Al_2O_3 catalyst was 1:9. In each test, 100 mg of soot–catalyst mixture was tightly packed between the discharge gap and held by quartz wool. For all experiments in this work, the DBD reactor was placed

in an oven (Lichen Tech., Shanghai, China), and the heating temperature was regulated between 25 °C and 180 °C with an accuracy of ±1 °C. The plasma discharge was initiated after the reaction temperature reached steady state.

All the electrical signals were recorded by a Tektronix TDS2024C oscilloscope, and the discharge power was calculated using the Lissajous method. The whole process of plasma–catalytic soot oxidation was performed for 30 min, while the concentrations of major gaseous products of CO and CO_2 were measured by an on-line infrared gas analyzer (GXH-3010/3011AE, Huayun, China) with an accuracy of ±3%. All experiments were performed three times, and the average values are presented. The reaction performance was evaluated considering the soot oxidation rate and CO_2 selectivity of the process, which were calculated as follows:

$$m_{soot} = \frac{Q \times \int_0^t (c_{CO} + c_{CO_2})dt}{V_m} \times M_c \quad (7)$$

$$m_{soot} = \frac{Q \times \int_0^t (c_{CO} + c_{CO_2})dt}{V_m} \times M_c \quad (8)$$

$$CO_2 selectivity(\%) = \frac{\int_0^t c_{CO_2} dt}{\int_0^t (c_{CO} + c_{CO_2})dt} \times 100\% \quad (9)$$

where m_{soot} is the weight of converted soot during the plasma–catalytic oxidation process, Q is the flow rate, V_m is the gas molar volume under experimental conditions, M_c is the molar mass of carbon, t is the reaction time, M_{soot} is the weight of initially packed soot, and c_{co} and c_{co2} are CO and CO_2 concentrations in the effluent, respectively.

4. Conclusions

In the presented work, plasma–catalytic soot oxidation was conducted over a series Mn-X/γ-Al_2O_3 (X = Ce, Co and Cu) catalysts. The doping of Ce, Co and Cu species slightly decreased the soot oxidation rate compared with Mn/γ-Al_2O_3, while the order of soot oxidation was in the order of Mn/γ-Al_2O_3 (57.7%) > Mn-Co/γ-Al_2O_3 (53.9%) > Mn-Ce/γ-Al_2O_3 (51.6%) > Mn-Cu/γ-Al_2O_3 (47.7%) during the 30 min soot oxidation process at 150 °C. The CO_2 selectivity of the process was improved in the presence of dopants and followed the opposite order of oxidation rate.

Various catalyst characterizations, including N_2 adsorption–desorption, XRD, XPS, H_2-TPR and O_2-TPD, were performed to illustrate the structure–performance relationships of plasma–catalytic soot oxidation. High $O_{ads}/(O_{ads}+O_{latt})$ values of Mn-X/γ-Al_2O_3 catalysts indicated abundant oxygen vacancies on their surfaces, which was beneficial for the release of O_{ads} species during soot oxidation compared with Mn/γ-Al_2O_3. The lower reduction temperature of Mn-X/γ-Al_2O_3 also confirmed the feasibility of O_{ads} species activation over the catalysts, which could benefit the oxygen transfer from catalyst surfaces to soot particles. O_2-TPD showed that Mn-Co/γ-Al_2O_3 also possessed the most O_{ads} species on its surface. The order of reducibility of Mn-X/γ-Al_2O_3 catalysts was in line with the order of CO_2 selectivity of the process, and directly opposite that of the soot oxidation rate. The decrease in the soot oxidation rate could be attributed to the consumption of plasma-generated reactive species in the presence of a catalyst, while the improvement in CO_2 selectivity may be ascribed to the utilization of oxidative species, including O_{ads}, O and O_3, for the oxidation of -CO groups on soot surfaces via the interfaces between soot particles and catalyst pellets.

The effects of discharge power, oxygen content in the carrier gas and reaction temperature on plasma–catalytic soot oxidation were systematically analyzed. The results show that a higher discharge power and lower oxygen content and reaction temperature were beneficial for soot oxidation, while the CO_2 selectivity of the process under these working conditions would be inhibited.

The results obtained in this work could help us to further design and optimize the plasma-catalytic instrument for soot oxidation in terms of catalyst composition, contact type and the screening of proper working conditions. More importantly, it should be noted that the present work mainly focused on the feasibility of using Mn-based catalysts for plasma–catalytic soot oxidation at the lab scale. The future work should be designed to be able to cope with the real conditions of DPF regeneration, i.e., the contact type between soot and catalysts, the design of catalyst composition, the distribution of active metal catalysts on the support, loading method and number of catalysts on the real DPF should be considered. Besides the catalysts, the configuration of plasma reactor structure, types of discharge power and the working conditions are also very important.

Author Contributions: Conceptualization, X.Z. and G.C.; Data curation, X.W.; Formal analysis, X.Z., X.W. and Z.Y.; Funding acquisition, X.Z.; Investigation, X.W., J.L. (Jianbin Luo) and Y.J.; Methodology, X.W., J.L. (Jin Liu) and Y.J.; Resources, X.Z.; Writing—original draft, X.Z. and J.L. (Jin Liu); Writing—review and editing, X.Z. All authors have read and agreed to the published version of the manuscript.

Funding: This work was funded by the National Natural Science Foundation of China (No. 51976093), the K.C. Wong Magna Fund in Ningbo University and the Qingdao science and technology demonstration and guidance project for benefiting the people (No. 21-1-4-sf-8-nsh).

Data Availability Statement: The data presented in this study are available on request from the corresponding author.

Acknowledgments: Xinbo Zhu would like to thank the support from the National Natural Science Foundation of China (No. 51976093) and the K.C. Wong Magna Fund from Ningbo University. Ye Jiang and Zhengda Yang are funded by the Qingdao science and technology demonstration and guidance project for benefiting the people (No. 21-1-4-sf-8-nsh).

Conflicts of Interest: The authors declare no conflict of interest.

References

1. Feng, S.; Xu, S.; Yuan, P.; Xing, Y.; Shen, B.; Li, Z.; Zhang, C.; Wang, X.; Wang, Z.; Ma, J.; et al. The impact of alternative fuels on ship engine emissions and aftertreatment systems: A review. *Catalysts* **2022**, *12*, 138. [CrossRef]
2. Liati, A.; Dimopoulos Eggenschwiler, P.; Schreiber, D.; Zelenay, V.; Ammann, M. Variations in diesel soot reactivity along the exhaust after-treatment system, based on the morphology and nanostructure of primary soot particles. *Combust. Flame* **2013**, *160*, 671–681. [CrossRef]
3. Lisi, L.; Landi, G.; Di Sarli, V. The issue of soot-catalyst contact in regeneration of catalytic diesel particulate filters: A critical review. *Catalysts* **2021**, *10*, 1307. [CrossRef]
4. Landi, G.; Di Sarli, V.; Lisi, L. A numerical investigation of the combined effects of initial temperature and catalyst activity on the dynamics of soot combustion in a catalytic diesel particulate filter. *Top. Catal.* **2021**, *64*, 270–287. [CrossRef]
5. Di Sarli, V.; Landi, G.; Di Benedetto, A.; Lisi, L. Synergy between ceria and metals (Ag or Cu) in catalytic diesel particulate filters: Effect of the metal content and of the preparation method on the regeneration performance. *Top. Catal.* **2020**, *64*, 256–269. [CrossRef]
6. Palma, V.; Ciambelli, P.; Meloni, E.; Sin, A. Catalytic DPF microwave assisted active regeneration. *Fuel* **2015**, *140*, 50–61. [CrossRef]
7. Caliskan, H.; Mori, K. Environmental, enviroeconomic and enhanced thermodynamic analyses of a diesel engine with diesel oxidation catalyst (DOC) and diesel particulate filter (DPF) after treatment systems. *Energy* **2017**, *128*, 128–144. [CrossRef]
8. Lin, H.; Huang, Z.; Shangguan, W.F. Temperature-programmed oxidation of soot in a hybrid catalysis-plasma system. *Chem. Eng. Technol.* **2008**, *31*, 110–115. [CrossRef]
9. Shi, Y.; Cai, Y.; Fan, R.; Cui, Y.; Chen, Y.; Ji, L. Characterization of soot inside a diesel particulate filter during a nonthermal plasma promoted regeneration step. *Appl. Therm. Eng.* **2019**, *150*, 612–619. [CrossRef]
10. Ranji-Burachaloo, H.; Masoomi-Godarzi, S.; Khodadadi, A.A.; Mortazavi, Y. Synergetic effects of plasma and metal oxide catalysts on diesel soot oxidation. *Appl. Catal. B Environ.* **2016**, *182*, 74–84. [CrossRef]
11. Pu, X.; Cai, Y.; Shi, Y.; Wang, J.; Gu, L.; Tian, J.; Li, W. Diesel particulate filter (DPF) regeneration using non-thermal plasma induced by dielectric barrier discharge. *J. Energy Inst.* **2018**, *91*, 655–667. [CrossRef]
12. Sekine, Y.; Koyama, H.; Matsukata, M.; Kikuchi, E. Plasma-assisted oxidation of carbon particle by lattice oxygen on/in oxide catalyst. *Fuel* **2013**, *103*, 2–6. [CrossRef]
13. Bogaerts, A.; Tu, X.; Whitehead, J.C.; Centi, G.; Lefferts, L.; Guaitella, O.; Azzolina-Jury, F.; Kim, H.-H.; Murphy, A.B.; Schneider, W.F.; et al. The 2020 plasma catalysis roadmap. *J. Phys. D Appl. Phys.* **2020**, *53*, 443001. [CrossRef]

14. Guo, H.; Yang, H.; Huang, J.; Tong, J.; Liu, X.; Wang, Y.; Qiao, W.; Han, J. Theoretical and experimental insight into plasma-catalytic degradation of aqueous p-nitrophenol with graphene-Zno nanoparticles. *Sep. Purif. Technol.* **2022**, *295*, 121362. [CrossRef]
15. Liu, S.; Liu, Y.; Tang, D.; Miao, Y.; Cao, Z.; Zhao, Z. Synergy of NTP-$La_{1-x}Ag_xMn_{1-y}Co_yO_{3-\delta}$ hybrid for soot catalytic combustion at low temperature. *Plasma Chem. Plasma Process.* **2021**, *41*, 1009–1019. [CrossRef]
16. Ding, S.; Zhu, C.; Hojo, H.; Einaga, H. Enhanced catalytic performance of spinel-type Cu-Mn oxides for benzene oxidation under microwave irradiation. *J. Hazard. Mater.* **2022**, *424*, 127523. [CrossRef]
17. Wang, M.; Zhang, Y.; Yu, Y.; Shan, W.; He, H. Surface oxygen species essential for the catalytic activity of Ce–M–Sn (M = Mn or Fe) in soot oxidation. *Catal. Sci. Technol.* **2021**, *11*, 895–903. [CrossRef]
18. Chen, L.; Liu, G.; Feng, N.; Yu, J.; Meng, J.; Fang, F.; Zhao, P.; Wang, L.; Wan, H.; Guan, G. Effect of calcination temperature on structural properties and catalytic soot combustion activity of MnO_x/wire-mesh monoliths. *Appl. Surf. Sci.* **2019**, *467*, 1088–1103. [CrossRef]
19. Yu, D.; Peng, C.; Yu, X.; Wang, L.; Li, K.; Zhao, Z.; Li, Z. Facile preparation of amorphous Ce_nMnO_x catalysts and their good catalytic performance for soot combustion. *Fuel* **2022**, *307*, 121803. [CrossRef]
20. Liu, L.-J.; Li, X.-X.; Wang, H.; Xue, B.; Zheng, X.-M.; Chen, M. Application of combined plasma-catalytic method for carbon particulate matter (PM) removal. *RSC Adv.* **2015**, *5*, 40012–40017. [CrossRef]
21. Lippens, B.C.; De Boer, J. Studies on pore systems in catalysts: V. The t method. *J. Catal.* **1965**, *4*, 319–323.
22. Sing, K.S. Reporting physisorption data for gas/solid systems with special reference to the determination of surface area and porosity (recommendations 1984). *Pure Appl. Chem.* **1985**, *57*, 603–619. [CrossRef]
23. Zakaria, Z.Y.; Linnekoski, J.; Amin, N.A.S. Catalyst screening for conversion of glycerol to light olefins. *Chem. Eng. J.* **2012**, *207*, 803–813. [CrossRef]
24. Zhu, X.; Gao, X.; Yu, X.; Zheng, C.; Tu, X. Catalyst screening for acetone removal in a single-stage plasma-catalysis system. *Catal. Today* **2015**, *256*, 108–114. [CrossRef]
25. Wang, L.; He, H.; Zhang, C.; Wang, Y.; Zhang, B. Effects of precursors for manganese-loaded γ-Al_2O_3 catalysts on plasma-catalytic removal of o-xylene. *Chem. Eng. J.* **2016**, *288*, 406–413. [CrossRef]
26. Zhang, J.; Yao, X.; Shao, Q.; Xu, B.; Liang, X.; Long, C. Nonthermal plasma-assisted catalytic oxidation of carbon monoxide over CuO_x@γ-Al_2O_3: Understanding plasma modification of catalysts and plasma-catalyst synergy. *J. Phys. Chem. C* **2019**, *123*, 16721–16730. [CrossRef]
27. Zhang, F.; Zhu, X.; Wu, H.; Wu, X.; Zhou, Z.; Chen, G.; Yang, G. Activity and stability of Cu-based spinel-type complex oxides for diesel soot combustion. *ChemistrySelect* **2021**, *6*, 14019–14026. [CrossRef]
28. Xu, J.; Liu, J.; Zhao, Z.; Xu, C.; Zheng, J.; Duan, A.; Jiang, G. Easy synthesis of three-dimensionally ordered macroporous $La_{1-x}K_xCoO_3$ catalysts and their high activities for the catalytic combustion of soot. *J. Catal.* **2011**, *282*, 1–12. [CrossRef]
29. Han, Y.-F.; Zhong, Z.; Ramesh, K.; Chen, F.; Chen, L. Effects of different types of γ-Al_2O_3 on the activity of gold nanoparticles for CO oxidation at low-temperatures. *J. Phys. Chem. C* **2007**, *111*, 3163–3170. [CrossRef]
30. Mobini, S.; Meshkani, F.; Rezaei, M. Supported Mn catalysts and the role of different supports in the catalytic oxidation of carbon monoxide. *Chem. Eng. Sci.* **2019**, *197*, 37–51. [CrossRef]
31. Zhao, H.; Li, H.; Pan, Z.; Feng, F.; Gu, Y.; Du, J.; Zhao, Y. Design of CeMnCu ternary mixed oxides as soot combustion catalysts based on optimized Ce/Mn and Mn/Cu ratios in binary mixed oxides. *Appl. Catal. B Environ.* **2020**, *268*, 118422. [CrossRef]
32. Dosa, M.; Piumetti, M.; Bensaid, S.; Andana, T.; Novara, C.; Giorgis, F.; Fino, D.; Russo, N. Novel Mn-Cu-containing CeO_2 nanopolyhedra for the oxidation of CO and diesel soot: Effect of dopants on the nanostructure and catalytic activity. *Catal. Lett.* **2018**, *148*, 298–311. [CrossRef]
33. Zhang, S.; Zhu, X.; Zheng, C.; Hu, D.; Zhang, J.; Gao, X. Study on catalytic soot oxidation over spinel type ACo_2O_4 (A = Co, Ni, Cu, Zn) catalysts. *Aerosol Air Qual. Res.* **2017**, *17*, 2317–2327. [CrossRef]
34. Lee, J.H.; Lee, B.J.; Lee, D.-W.; Choung, J.W.; Kim, C.H.; Lee, K.-Y. Synergistic effect of Cu on a Ag-loaded CeO_2 catalyst for soot oxidation with improved generation of active oxygen species and reducibility. *Fuel* **2020**, *275*, 117930. [CrossRef]
35. Guan, B.; Huang, Y.; Lin, H.; Huang, Z. Promoting effects of barium substitution on the catalytic performances of $FeCeO_{2-\delta}$ for soot oxidation. *Ind. Eng. Chem. Res.* **2018**, *57*, 8635–8646. [CrossRef]
36. Wu, H.; Zhu, X.; Wu, X.; Tu, X.; Chen, G.; Yang, G. Plasma-catalytic reactions for soot oxidation on VO_x/M (M=KIT-6, SBA-15 and SiO_2) catalysts: Influence of pore structure. *ChemistrySelect* **2022**, *7*, e202103545. [CrossRef]
37. Tu, X.; Whitehead, J.C. Plasma dry reforming of methane in an atmospheric pressure AC gliding arc discharge: Co-generation of syngas and carbon nanomaterials. *Inter. J. Hydro. Energy* **2014**, *39*, 9658–9669. [CrossRef]
38. Whitehead, J.C. Plasma–catalysis: The known knowns, the known unknowns and the unknown unknowns. *J. Phys. D Appl. Phys.* **2016**, *49*, 243001. [CrossRef]
39. Turns, S.R. *An Introduction to Combustion: Concepts and Applications*, 2nd ed.; McGraw-Hill Education: New York, NY, USA, 1985.
40. Yamamoto, S.; Yao, S.; Kodama, S.; Mine, C.; Fujioka, Y. Investigation of transition metal oxide catalysts for diesel pm removal under plasma discharge conditions. *Open Catal. J.* **2008**, *1*, 11–16. [CrossRef]
41. Wagloehner, S.; Kureti, S. Study on the mechanism of the oxidation of soot on Fe_2O_3 catalyst. *Appl. Catal. B Environ.* **2012**, *125*, 158–165. [CrossRef]
42. López-Suárez, F.E.; Bueno-López, A.; Illán-Gómez, M.J. Cu/Al_2O_3 catalysts for soot oxidation: Copper loading effect. *Appl. Catal. B Environ.* **2008**, *84*, 651–658. [CrossRef]

43. Liu, Y.; Lian, L.; Zhao, W.; Zhang, R.; Hou, H. DBD coupled with MnO_x/γ-Al_2O_3 catalysts for the degradation of chlorobenzene. *Plasma Sci. Technol.* **2020**, *22*, 034016. [CrossRef]
44. Zhu, X.; Zhang, S.; Yang, Y.; Zheng, C.; Zhou, J.; Gao, X.; Tu, X. Enhanced performance for plasma-catalytic oxidation of ethyl acetate over $La_{1-x}Ce_xCoO_{3+\delta}$ catalysts. *Appl. Catal. B Environ.* **2017**, *213*, 97–105. [CrossRef]
45. Wagloehner, S.; Nitzer-Noski, M.; Kureti, S. Oxidation of soot on manganese oxide catalysts. *Chem. Eng. J.* **2015**, *259*, 492–504. [CrossRef]
46. Guilhaume, N.; Bassou, B.; Bergeret, G.; Bianchi, D.; Bosselet, F.; Desmartin-Chomel, A.; Jouguet, B.; Mirodatos, C. In situ investigation of diesel soot combustion over an $AgMnO_x$ catalyst. *Appl. Catal. B Environ.* **2012**, *119–120*, 287–296. [CrossRef]
47. Peng, X.S.; Lin, H.; Shangguan, W.F.; Huang, Z. Surface properties and catalytic performance of $La_{0.8}K_{0.2}Cu_xMn_{1-x}O_3$ for simultaneous removal of NOx and soot. *Chem. Eng. Technol.* **2007**, *30*, 99–104.
48. Chen, G.; Tu, X.; Homm, G.; Weidenkaff, A. Plasma pyrolysis for a sustainable hydrogen economy. *Nat. Rev. Mater.* **2022**, *7*, 333–334. [CrossRef]
49. Zhang, X.; Ren, B.; Xu, Y.; Li, X.; Yu, P.; Sun, Y.; Zheng, H. Catalytic oxidation of toluene in air using manganese incorporated catalyst by non-thermal plasma system. *Sep. Purif. Technol.* **2021**, *257*, 117973. [CrossRef]
50. Zhang, H.; Li, K.; Shu, C.; Lou, Z.; Sun, T.; Jia, J. Enhancement of styrene removal using a novel double-tube dielectric barrier discharge (DDBD) reactor. *Chem. Eng. J.* **2014**, *256*, 107–118. [CrossRef]
51. Fridman, A.A. *Plasma Chemistry*; Cambridge University Press: Cambridge, UK, 2008.
52. Ogata, A.; Saito, K.; Kim, H.H.; Sugasawa, M.; Aritani, H.; Einaga, H. Performance of an ozone decomposition catalyst in hybrid plasma reactors for volatile organic compound removal. *Plasma Chem. Plasma Process.* **2010**, *30*, 33–42. [CrossRef]
53. Blin-Simiand, N.; Jorand, F.; Belhadj-Miled, Z.; Pasquiers, S.; Postel, C. Influence of temperature on the removal of toluene by dielectric barrier discharge. *Int. J. Plasma Environ. Sci. Technol.* **2007**, *1*, 64–70.
54. Huang, J.; Puyang, C.; Guo, H. Sodium percarbonate activation by plasma-generated ozone for catalytic degradation of dye wastewater: Role of active species and degradation process. *Catalysts* **2022**, *12*, 681. [CrossRef]